STRAIN-BASED HEALTH INDICATORS FOR THE STRUCTURAL HEALTH MONITORING OF STIFFENED COMPOSITE PANELS

DIMITRIOS P. MILANOSKI AND THEODOROS H. LOUTAS

Laboratory of Applied Mechanics and Vibrations
Dept. of Mechanical Engineering and Aeronautics, University of Patras
Patras University Campus, GR-26504, Rio-Patras, Greece
Corresponding author: T. Loutas Email: thloutas@upatras.gr

Key words: Parametric finite element model, skin/stringer disbonding, structural health monitoring, strain field, non-linear buckling analysis.

Abstract. A common defect of composite stiffened structures is the disbond at the interface between the two constituents (skin/stringer), as a result of inefficient manufacturing process or foreign object impacts in service. Generally, discontinuities within the volume of an elastic solid medium subjected to mechanical load, cause anomalies on the strain field in the near vicinity of the discontinuity. Utilizing this observation, the current work investigates the effect of artificially induced disbonds in the skin/stiffener interface of an aeronautical grade generic element. A structural health monitoring methodology is developed, leveraging on numerically simulated strains along the stringer foot which aims to assess the health state of the panel as the size of the disbonds increases. The study is implemented with a parametric finite element model generating various disbond scenarios. Longitudinal strain values are acquired at the exact points where in reality actual Fiber Bragg Grating sensors will be located. Two types of commonly utilized strain-based Health Indicators are evaluated, and their drawbacks are revealed and discussed. A new Health Indicator is proposed that proves its capability to monitor growing disbonds being at the same time load and baseline independent.

1. Introduction

Primary airframe structures made of composites tend to increasingly replace more conventional materials. Their advantages correlate to the high specific mechanical properties over metallic materials. Nevertheless, these materials suffer from hidden damages, such delaminations/disbonds which arise major concerns if not identified at an early stage. In this direction, researchers utilize Structural Health Monitoring (SHM) technologies to identify and assess damage. SHM systems elaborate an adequate array of physical measurements via permanently installed sensors, in order to deduce any abnormality with respect to the pristine state of the monitored structure. Sensor readings may not directly associate to damage (Worden et al., 2007). Proper data processing should evaluate which are the damage sensitive Health Indicators (HIs) that can effectively monitor growing damage. Strain-based SHM as

realized through Fiber optic sensors (FOS) technology has gained increasing popularity as an innovative method of real-time strain measurements during service with minimum additive weight. A popular category of FOS is the Fiber Bragg grating sensors (FBGs) (Hill and Meltz, 1997). Quite a few researchers developed health monitoring methodologies based on this type of sensors for example Li et al. (2004), who investigated the strain field modification along interfacial disbonds that existed amidst the bond-line of adhesively bonded GFRP joints. The specimens were subjected to in-plane shear and through-thickness tension. Both virtual and experimental strains revealed the strain disturbance along the disbonds. An automated algorithm for damage detection and quantification was proposed in Li et al. (2006a), which was validated on naval composite T-joint specimens. A strain-residual baseline of the pristine specimen was developed for training purposes and via a statistical outlier analysis, disbond cases were qualitatively detected. Experimental static strains were received by embedded FBGs. Li et al. (2006b) employed a strain differential approach to estimate the effect of disbonds to the strain distribution of two types of composite repairs. A finite element modeling methodology was developed accompanied with experimental strain measurements and finally a “threat factor” was proposed to assess the health state of the repairs. A study based on static strains was implemented in a relevant work (Fernández-López et al., 2007). Two closely placed optical fibers with FBGs were bonded to the skin and the edge of the stringer respectively. In this case, the differential strain of closely attached sensors placed away from damage, maintained a linear relation with respect to a reference strain, while sensors closest to damage showed a non-linear behavior. Another investigation on a composite single-lap specimen with GFRP adherents subjected to cyclic load was conducted by (Palaniappan et al., 2008). Chirped FBGs were used to monitor disbond initiation and subsequent growth in the adjacent region of the overlap. Similarly, a disbond monitoring methodology was experimentally evaluated for CFRP double-lap joints operating in cyclic load (Yashiro et al., 2017). Embedded FBGs crossing the area of the double-lap joint yielded a two-peak reflected spectrum and the authors proposed a peak-intensity ratio based on the two formed peaks. Leveraging on a finite element analysis, the relation of the peak-intensity ratio to the disbond size showed a gradual increase. Interlaminar damage occurred by low-velocity impacts on CFRP stiffened panels was investigated by Takeda et al. (2012). They used embedded FBGs to monitor the shift on the central wavelength of the reflected spectra when the panel was subjected to uniaxial compression after impact. They furtherly reported a significant divergence on the measured strains at the post-buckling region, between intact and damaged panels, via FBGs placed close to the impact locations.

Loutas et al. (2015) developed a methodology for the optical fiber placement, in order to ease the handling and surface attachment. The designated fiber optic ribbon tape efficiently recorded strains during fatigue loading, indicating reliable measurements over an extended operating spectrum of 10^6 duty cycles. A framework utilizing the aforementioned ribbon tapes was proposed by (Airoldi et al., 2015). An integrated Health and Usage Monitoring System (HUMS) of composite spars belonging to a wing-box was developed, aiming to monitor load as well as damage severity. In the work of Ciminello et al. (2017) the skin-to-spar bonding failure on a winglet was investigated. FBGs were placed along the maximum excitation

direction as this derived from a preliminary finite element analysis. Short Time Fast Fourier Transform was employed to the experimental strains induced by cyclic load, in order to reveal damage occurrences. Strain-based damage detection methodologies also form an attractive solution for the wind energy section (Tian et al., 2015). An algorithm was confirmed on the prediction of hidden delaminations in a wing turbine blade, based on static strains monitored via FBGs mounted on its surface.

Other researchers utilized data-oriented methodologies towards health monitoring. A new method to identify strain modification along disbonds exploiting Artificial Neural Networks (ANNs) was proposed by Kesavan and co-authors (2008). The existence and extent of various disbond configurations were sufficiently predicted relying on the induced strain distributions along the width of the joint's foot. Later, a model-based approach relying on data derived from numerical modelling was presented (Katsikeros and Labeas, 2009). A finite element model of a riveted lap-joint was created, incorporating unidimensional cracks starting from the rivet holes' borders. Training of the neural net was achieved utilizing a strain-based damage index as it was calculated using strain data of the model. Crack monitoring was made on the basis of comparing the strain distribution between the riveted region and a remote one, alleviated by strain-concentrations, in the far field of the joint. A similar model-based methodology was designed (Sbarufatti et al., 2013), leveraging on a global-local finite element model of a helicopter tail boom in order to evaluate realistic fatigue crack propagation events. Damage detection was enabled by utilizing the Mahalanobis distance, considering a damage index calculated at each sensor spot. The methodology was validated experimentally using permanently placed FBGs to record strain data. An upgraded framework of the latter work was composed (Salvetti et al., 2019), introducing cointegration as a new novel method of data normalization. Continuously growth phenomena of fatigue-induced cracks were efficiently monitored via two experimental campaigns, using real-time strain measurements recorded from a network of FBGs. An innovative damage detection methodology (Sierra-Pérez et al., 2014) based on Principal Component Analysis (PCA) was also proposed. Damage indices T^2 and Q were calculated based on FBG measurements on the wing section of an unnamed air vehicle. This methodology eliminated the load dependency of the strain readings resulting accurate predictions of damages under variable loading conditions. Several studies have utilized dynamic strains towards SHM see for example Panopoulou et al. (2012) where a composite stiffened panel incorporating various structural damages, in terms of lumped masses fixed to its surface, was assessed. A cross-validated ANN was used for damage identification and localization based on features extracted from the dynamic strains.

An additional well-established metrological technology of FOS is distributed sensing (Güemes et al., 2010). The optical fiber does not need to have any engraved sensors and they provide strain readings with a much denser spatial resolution than FBGs. Researchers from several fields showed an intense interest on SHM applications utilizing distributing sensing technique over the last years (Glisic and Inaudi, 2012; Romano et al., 2019). A non-model-based SHM system was proposed by (Ciminello et al., 2018). A distributed sensing optical fiber was attached on the surface of a composite stiffened panel with a Kapton tape. Damage detection was established utilizing a "dispersion feature" vector algorithm based on the strain

signal received by the fiber. They reported maximum error on the detection of the disbond length of approximately 5 cm. Also, another work (Shan et al., 2019) used as a strain acquisition technique a distributed sensing optical fiber. A damage index is suggested exploiting the dense arrangement of measuring segments along the fiber. Essentially, this damage index can detect abrupt changes in the strain gradient, a common evidence in the vicinity of induced flaws. Evaluation of the proposed methodology was conducted via a large-scale test on a composite winglet.

The objective and the contribution of the present paper is to study the effect of disbondings/delaminations in the strain-field developed at the stringers feet of T-joint single-stiffener panels (SSPs) and propose strain-based and load-independent Health Indicators capable of identifying and monitoring damage of growing size. The approach of this study is confined in a numerical framework. Parametric numerical modeling and virtual testing, i.e. quasi-static axial compression, are implemented to this direction. Initially, strains along the feet of defected models are directly compared with those of the pristine model. We show that this commonly adopted approach rises limitations based on the intrinsic dependency of the induced strain to load, i.e. the strains have to be compared at the exact same load level. Subsequently, a second indicator, which has been previously utilized for the monitoring of growing unidimensional cracks, is evaluated for our case study. Although, this indicator strongly depended on the load when the structure transcended its buckling load. To overcome this hindrance a novel health indicator is proposed, leveraging on the anti-symmetrically formed buckling mode of the structure, and numerically evaluated for its disbonding detection capabilities at the post-buckling regime of a composite single-stiffener panel (SSP).

2. Numerical modeling

The numerical modeling procedure is presented in the following chapter. First, the SSP specimen is introduced and its geometrical characteristics are detailed. The test article consists of two individual parts, a thin composite flat plate, the skin and a composite T-section stringer. The present study investigates the distribution of longitudinal static strains on the outer surface of each stringer foot in healthy and defected scenarios. Interrogation points are selected in a manner to simulate permanently installed sensors, such as Bragg grating sensors, in pre-selected locations. The macroscopic behavior of the pristine model will be indirectly validated based on an analytical formulation (Bisagni and Vescovini, 2009). This theory determines the initial stiffness and the bifurcation point of multi-stiffened composite panels subjected to uniaxial compression. Material, cross-sectional areas and generally the numerical analysis' details will be aligned with our single-stiffener panel. Finally, a parametric finite element model is created utilizing Python® scripting, simulating several disbond cases (i.e. sizes and locations), in order to assist the objective of this study. Further details regarding the parameterized way of modeling are given below.

2.1 Single-Stiffener Panel configuration

The geometrical dimensions of the SSP, expressed in *mm* are provided in Figure 1, accompanied by the stacking sequence of each member. The material used in this study is an IM7/8552 carbon/epoxy unidirectional continuum fiber-reinforced prepreg, with nominal cured ply thickness 0.131 mm (Hexcel Corporation, 2016) and mechanical properties adopted from Bisagni et al. (2010) and detailed in Table 1. From a numerical analysis point of view, the final geometry of the two members is modelled considering a co-curing manufacturing technique, without introducing an adhesive film in the interfacial region.

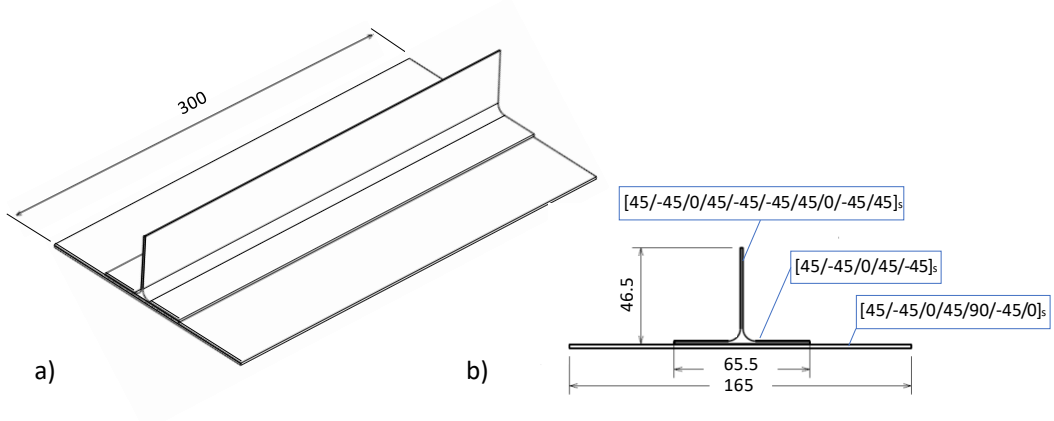

Figure 1. Dimensions of SSP specimen, a) 3D perspective and b) cross-sectional view

Table 1. Engineering and interlaminar properties of IM7/8552

Property	Value	Units
Longitudinal Young modulus	150	GPa
Transverse Young modulus	9.08	GPa
In-plane shear modulus	5.29	GPa
In-plane Poisson ratio	0.32	-
Mode-I critical energy release rate	0.277	N/mm
Mode-II critical energy release rate	0.788	N/mm
Mode-III critical energy release rate	0.788	N/mm
B-K exponent	1.6	-

2.2 Finite Element Model

The numerical model created, simulates the quasi-static compression of the pre-defined SSP. The SSP is loaded under displacement control, in an attempt to simulate a real test procedure. The load level plays a dominant role on the strain-based SHM methodologies. In the current analysis, the load is divided in 100 increments. A schematic illustration of the test article is showed in Figure 2, indicating also the two sensorized regions on the two feet (noted

as “Sensor Tape”) where strains will be measured experimentally with five FBGs in each. Also, the region that the disbond will be iteratively generated via the parametric model is highlighted by giving the initial and final position of the central axis (c.a.) of the generated disbonds.

The numerical study was implemented using the commercial finite element code Abaqus/Standard®. Both members are modelled as one layer of 4-node quadrilateral shell elements with reduced integration (S4R) and three integration points along the thickness. Every layer of composite laminates was modelled as a transverse isotropic material, according to the properties presented at Table 1, with thickness equal to the cured ply thickness the material provider suggests. Earlier experimental works highlighted that degradation of the material properties is negligible in the early post-buckling region (Dávila and Bisagni, 2017). Thus, for the numerical modeling tasks associated with the present study, progressive degradation of the material properties and intralaminar damage initiation/evolution were neglected. Instead of explicitly modeling the tabs, equivalent boundary conditions (BCs) have been imposed to the associated partitions. On the support tab region, all six nodal degrees of freedom have been restrained, while on the loading one, the only degree set free is the spatial displacement U_z. Displacement control condition was applied on the loading tab region. Among the individual constituents i.e. the skin and the stringer, tie constraints were applied to their surfaces to guarantee common interface degrees of freedom and thus common kinematics. Regarding the strain interrogation points, each FBG was numerically represented by a row of nodes with overall 10 mm length, as the FBGs we have used in previous experimental works. Thus, ten node sets were created mimicking the actual FBGs. In every location where the FBG sensor is designed to be placed, the average strain of the contained nodes is extracted and assumed as the strain reading of each sensor. In the present work the key point is not to model the principle of operation of the FBGs, but to numerically obtain virtual strains in a specific topology of measurement points assuming perfect strain transfer from the base material to the FBG. The node sets of the five FBGs per foot are labelled as RFBGs and LFBGs denoting the measurement regions belong to the right (RF) and left (LF) foot, respectively.

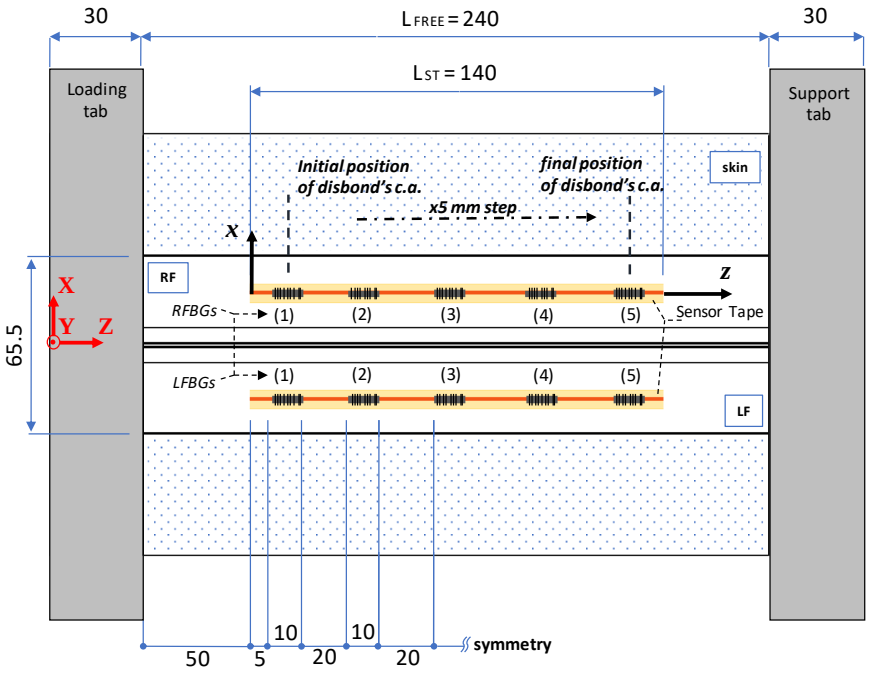

Figure 2. Conceptual design of sensorized specimen

The numerical analysis is divided in two steps. Initially, a linear buckling analysis is executed for the estimation of the buckling (eigen)modes and associated eigenvalues. A compressive unit load is applied which means that the eigenvalues express the critical buckling load with respect to the corresponding mode. Since linear perturbation analysis is not predicting stresses and strains but rather a normalized displacement field of the structure, a non-linear buckling analysis is compulsory. An important role is played by appropriate imperfections acting as triggering mechanism for the buckling initiation (bifurcation point). In general, two main categories of imperfections are considered in the literature (Zarouchas and Alderliesten, 2015) and described as:

- Normalized nodal displacements obtained via linear buckling analysis are introduced in the imminent non-linear analysis, following the pattern of the considering buckling modes
- A constant, low amplitude force acting along the buckling direction

The second method could alter the strain field in the adjacent region of the actuation point, while the first represents a more physical-based way to model the buckling behavior. In the present study, the first way of introducing imperfections is chosen, especially due to the need to obtain as much as possible reliable strain estimations. These imperfections in general are defined by superimposing multiple eigenmodes, and have the following amplitude form with respect to the global coordinate system:

$$\Delta x_i = \sum_{i=1}^{n} w_i \varphi_i \tag{1}$$

where w_i is the scale factor correlated with the i-th mode shape φ_i. Generally, the total response would be given by superimposing infinite terms of modes associated with a scale factor, although the lowest modes are frequently more critical. Experimental evidence on the buckling behavior of similar structures (Kolanu et al., 2018; Zou and Bisagni, 2018) showed that the first buckling eigenmode mainly dominate the macroscopic response. Thus, the first buckling mode shape was introduced and a scale factor equal to 5% of the skin's thickness was used. A static Newton-Raphson (N-R) solver, incorporating non-linear geometry formulation was utilized to solve the equilibrium system. An imposed displacement equal to 0.25 mm was set for loading BC at the top tab, as deep post-buckling analysis was not relevant with the current study. Due to such excitation, buckling occurred and was characterized by the non-linear relation between the reaction force and displacement of the panel. A mesh convergence study was implemented in a previous study of the authors (Milanoski and Loutas, 2019), regarding the buckling load as this was obtained from both linear and non-linear analysis. The load-displacement curve of the chosen mesh density is illustrated in Figure 3a. An approximate element size of 2.00 mm was selected producing a total discretization of 20550 elements, as shown in Figure 4a.

In order to estimate the validity of the numerical analysis, an analytical formulation (Bisagni and Vescovini, 2010) was utilized. This work reports a closed-form solution for the prediction of the buckling load of multi-stiffened panels, considering classical lamination theory assumptions while the stiffeners were modelled as torsion bars. Based on this, a blade-stiffened panel consisting of five stringers and a 200mm pitch distance between them is numerically modelled. The material properties, stacking sequence and the numerical parameters are identical with those in our study of the single-stringer panel. The nonlinear analysis derives an approximate 8.9% deviation in stiffness between the numerical analysis and the theory as presented in Figure 3b. A reason for this small discrepancy is that the presented theoretical methodology lies on the hypothesis of flexural isotropy, i.e. the components of the bending matrix which couple the bending and twisting deformation are null, $D_{16} = D_{26} = 0$, or negligible. Our layup shows a small flexural anisotropy in the layups of flange, web and skin as:

- Flange: D_{16}/D_{11} = 13.59 %
- Web: D_{16}/D_{11} = 3.21 %
- Skin: D_{16}/D_{11} = 10.24 %

Nevertheless, we can support it is not prohibitive to utilize the above analytical formulation in order to qualitatively validate the numerical modeling approach. Generally, differences between the finite element analysis and the theory rely on the fact that laminates with non-zero D_{16} and D_{26} values always produce buckling load lower than laminates without bending-

twisting coupling (Grenestedt, 1989). Also, both finite element analysis and the theory predicted skin buckling under 4 half waves along the longitudinal direction.

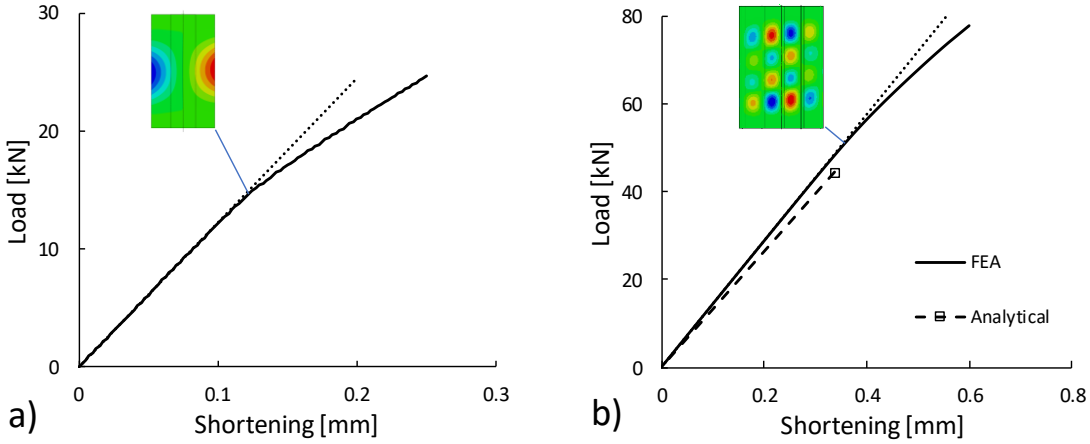

Figure 3. Load-shortening curves of a) single-stiffener and b) multi-stiffened panel

2.3 Parametric Analysis

The next task deals with the development of a parametric finite element model of the SSP with an artificially induced skin/stiffener, rectangle disbond. The parameterization concerns the position and the size of the disbond assuming a constant width (of 32.75mm) along the right foot alone, as shown in Figure 4b. We model disbonds spanning across half (or part) of the total width of the stiffener as more realistic than full width ones. In order to generate repetitive disbond scenarios at the skin/stiffener interface, a script written in Python® was elaborated. The advantage of this method was the easy applicability, while the script was executed directly via the interface of Abaqus®. The script was created on the basis of iteratively generating the geometry, including the parametric position and size of the disbond, while it entails all of the rest of the model attributes, as these have been previously described (material properties, mesh, BCs, etc.).

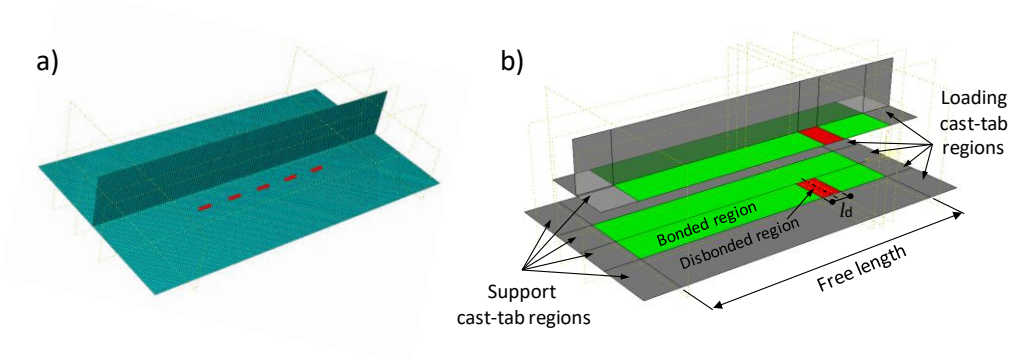

Figure 4. a) Discretized SSP, highlighting the RFBGs node sets, b) partitions of the SSP

As we described previously, tie constraints were introduced at the interface region between the skin and the stiffener. Modeling the disbond was achieved by erasing that interaction and allowing each of the individual regions of the disbond to freely move, without any kinematic constraint imposed by the other. The specimen was divided in partitions, in a manner of ensuring that coincident nodes at the interface of the two parts were generated. This approach prevented excessive distortion of the elements at the interface while it is mandatory for the implementation of the Virtual Crack Closure Technique (VCCT). In the current analysis, the VCCT was also used in order to assess if the disbonded regions do propagate under a specific loading condition. The interlaminar fracture properties of the IM7/8552 were used according to Table 1. Note that the VCCT is implemented by replacing the tie constraints with a contact interaction. This technique numerically calculates in every step the strain energy-release rate in a pre-defined crack/disbond front. For given critical strain energy-release rates of the material, the B-K criterion (Kenane and Benzaggagh, 1997) controls the fracture initiation and allows the front elements to separate if the criterion is satisfied. Also, the VCCT implementation requires to explicitly determine the unbonded region nodes in order to evaluate the strain energy release rate along the formed disbond fronts. This was also taken into consideration in the written script, so we can indicate two major node sets that were created per iteration as:

- one node set, representing the bonded region
- ten node sets, representing the FBGs along each foot

None of the considered analyses yield propagation of the associated disbond. A detailed flow chart describing the parametric implementation of the present work, is shown in Figure 5. After completion of every iteration, the disbond characteristics were updated, regarding either the position or the size.

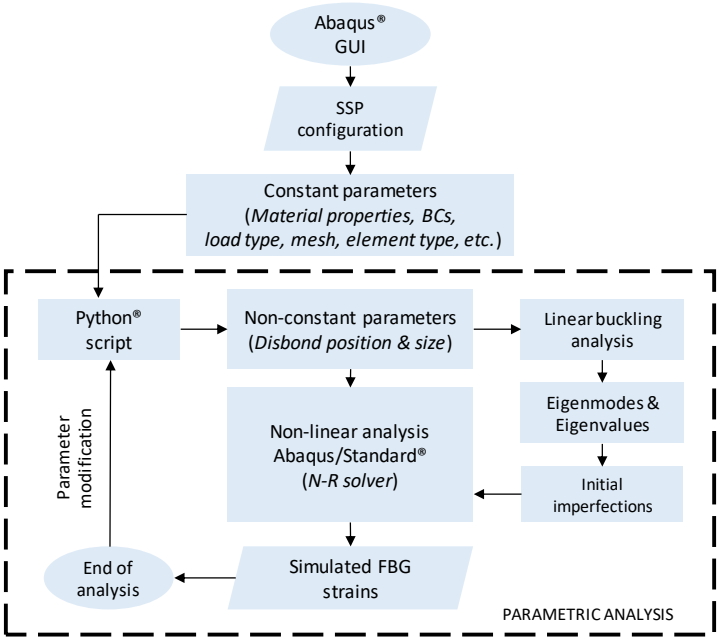

Figure 5. Explanation flow chart of the parametric analysis

3. Damage assessment of skin-to-stiffener disbond

In the current section, the effectiveness of HIs towards the detection of numerically simulated skin/stiffener disbonds will be investigated. The strain data obtained from the pristine specimen are considered as the baseline. Next, a SHM methodology based on the results obtained by the parametric analyses of skin-to-stiffener disbonds will be proposed and evaluated. As mentioned before, the parametric analysis generates models with a disbond in the interface of skin/stiffener, beneath the right foot. The assessment of disbonds, within the assumed sensor topology, initiated by introducing an HI to estimate the sensitivity of the FBGs to the disbond position via direct comparison of the static strains between the healthy and pristine/baseline conditions. In turn, the behavior of a second indicator was investigated versus the disbond size. The second indicator should utilize strains occurred at the linear response (prior buckling) of the panel. Finally, a new third HI which utilizes strain from both feet is proposed, in order to tackle the inefficiency of the second indicator in the early post-buckling regime.

3.1 Baseline SHM Methodology

The static strains obtained from the pristine specimen, as derived from the non-linear numerical analysis, establish the baseline which is utilized to reveal the presence of disbonds. Furthermore, regarding the disbond cases, similarly static strains at every FBG are gathered and stored, for each individual disbond scenario. The presence of an interfacial disbond region, affects the strain distribution along the foot. In order to visualize the effect of the disbonds, Figure 6 depicts the strain distribution along the path of the “Sensor Tape”, for both

pristine and two centrally-placed disbonds. The strain perturbation induced by the disbond can be clearly noticed along the right foot where the disbond exist. In turn, the distribution of the left foot does not show any perturbations as it is does not exhibit any structural defect. The maximum amplitude of the formed strain perturbation is spotted at the position of the disbond's central axis and presents an increasing trend proportional to the load. As the disbond changes position along the foot, analogous patterns of strain discrepancies were obtained following the disbond position. Moreover, the gradient and the amplitude of the strain discontinuity are not maintained constant and exhibit dependency both on the position and the load. In order to estimate the effect of the disbond to the strain modification, a Health Indicator (HI1) will be utilized based on the relative strain differences of every FBG node set in an arbitrary disbond case with the baseline. The HI forms a metric of the strain discrepancy between the baseline and the current condition, under the same load amplitudes and is calculated as shown in Eq. (2). As judiciously as we can imply, the comparison between strains induced due to the same loading is of high importance, otherwise the indicator correlates values irrelevant to each other and erroneous estimations will be deduced.

$$HI1_i = \left(\frac{\left| \varepsilon_{11}^{pristine} - \varepsilon_{11}^{disb} \right|}{\varepsilon_{11}^{pristine}} \right)_i, i = 1,2,\dots,5 \tag{2}$$

where *i* corresponds to the FBG number.

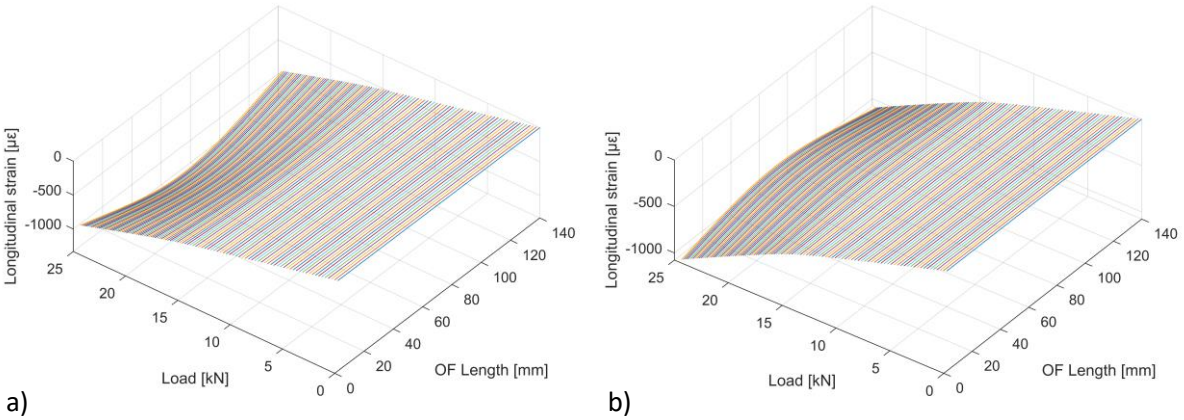

a) b)

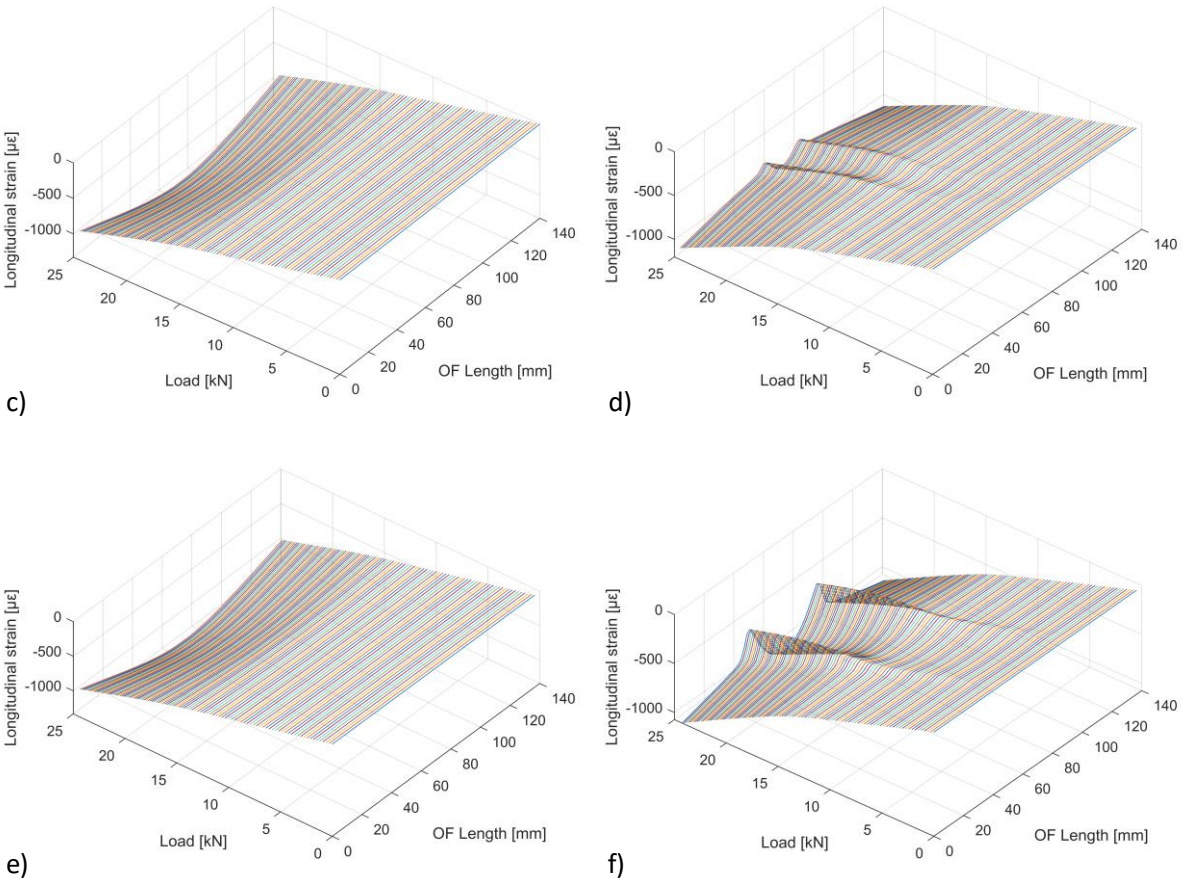

Figure 6. Simulated strain distributions along left foot (LF): a) Pristine, c) 25mm disbond, e) 50mm disbond and right foot (RF): b) Pristine, d) 25mm disbond and f) 50mm disbond

Indicatively, for two cases of constant disbond size 20 and 25 mm, the indicators of every FBG located at the right foot are calculated. Through the parametric numerical model, disbonds in a range of z = 10:130 mm are created, in the local coordinate system (*xyz*). The disbond position is incrementally increasing by 5 mm. The average HI1 is calculated for every FBG, and the results versus the disbond position are depicted in Figure 7. Error bars are used to denote the scattered values of the indicator as we consider several load levels in the range 0-25 kN. It can be seen that the indicators of every FBG-spot present an increase as the closer they are located to the central axis of the disbond. This observation enables the utilization of this indicator in order to conduct (strain) sensors optimal placement towards predicting the expedient number of sensors as well as their relative distance. Corresponding results of left foot are not presented as all of the sensors present negligible indications. This can also be validated via the unaffected strain distributions of the left foot, as shown in Figure 6.

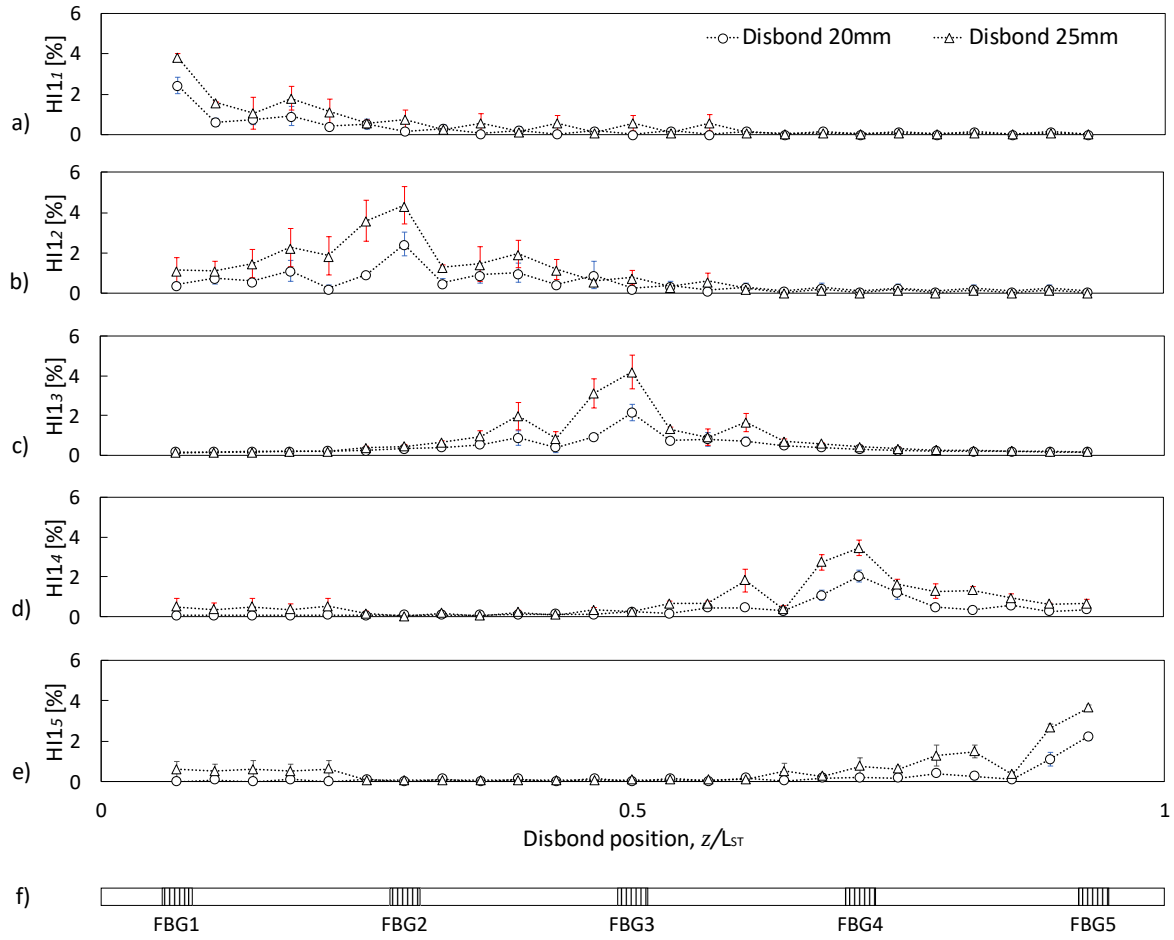

Figure 7. Average HI1 predicted by RFBG - a) 1, b) 2, c) 3, d) 4 and e) 5 versus the disbond position along RF. Error bars indicate the scatter due to changing load. f) Schematic representation of FBG positions

3.2 Growing disbond detection

Next, we utilize a second health indicator fit for Structural Health Monitoring, while the disbond size is parametrically growing. This HI combines the strain readings from all sensors per foot. In fact, it represents the percentage each FBG sensor holds from the cumulative strain among the five FBG sensors, and is defined as:

$$HI2_i = \frac{\varepsilon_{11}^i}{\frac{1}{n}\sum_i \varepsilon_{11}^i}, i = 1,2,\dots,n = 5 \tag{3}$$

where again *i* corresponds to FBG numbering of total (*n*=5) FBGs per foot. This HI is inspired by the observation that strains of the unaffected spots/sensors show minor deviation from the healthy strain indications. The same indicator used in earlier studies of monitoring

unidimensional cracks (Katsikeros and Labeas, 2009; Sbarufatti et al., 2013) as well as surface disbonds (Milanoski and Loutas, 2019). In order to study the dependency of the indicator to the load level, initially the HI is calculated for the pristine model in the whole range of loads, i.e. 0-25 kN (Figure 8). We can observe that the values of the indicator almost remain constant up to buckling, and when buckling occurred they yielded a gradual monotonicity. This observation declares that if the HI is envisaged to monitor the potential growth of the disbond, then it is limited only in the pre-buckling regime. Otherwise it is very dependent on the load. In Figure 9 the average values of the HI for every FBG at various loads are presented, implemented for RF disbond sizes up to 60mm, i.e. 25% of the total free length. Loads are considered prior to buckling. Error bars are not visible as their size is less than 1% in all of the points. Indicatively, the results concern the case of a growing disbond that is placed at the center of the RF. Utilizing the parametric finite element model, the disbond is equally increased from both ends along the longitudinal direction per iteration. The 3rd sensor on the RF is the most affected by the disbond and this fact is illustrated with a monotonical increase on its index of about 8% regarding the initial intact value. The rest FBG sensors show a coalescence of their values until the disbond reaches the adjacent to FBG-3 sensors, alternating their strains recordings, and finally we observe separation of their indications. On the contrary, it can be clearly noticed that HIs of the LF show no discrimination from the pristine case.

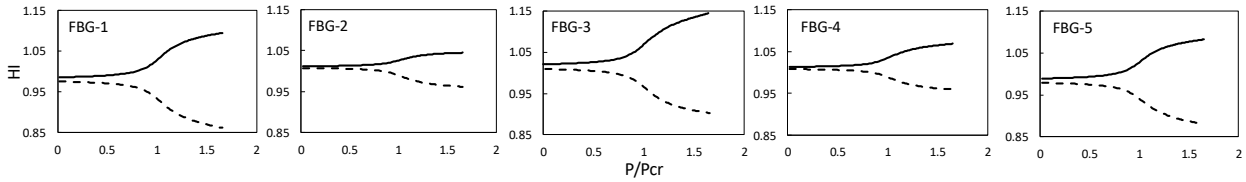

Figure 8. Evolution of the health indicator (pristine case) versus load level calculated at LF (--) and RF (-)

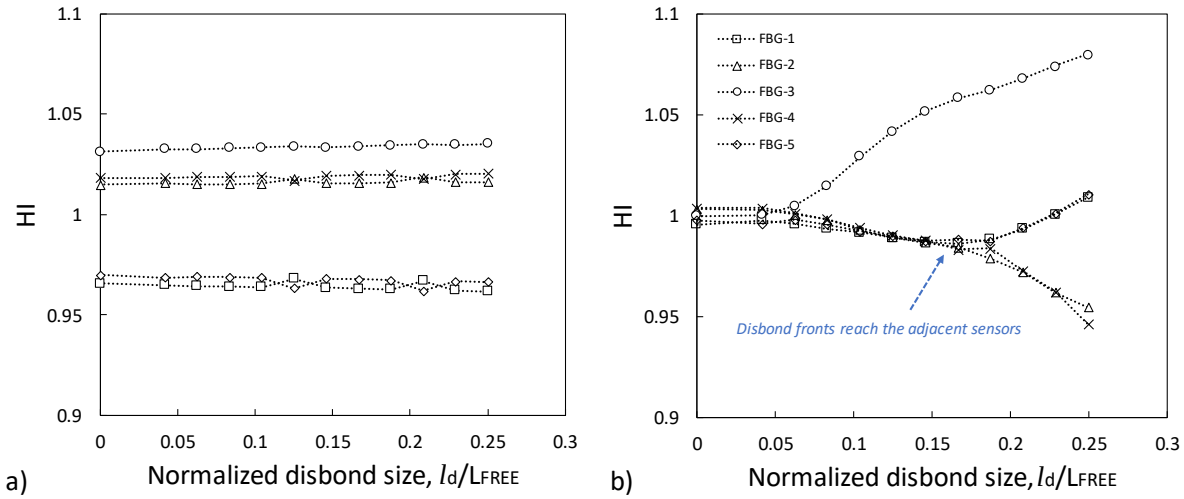

Figure 9. Average values of HI2 of all FBGs incorporating various disbond sizes calculated at a) LF and b) RF

Finally, in an attempt to overcome the limitation of the previous health indicator, we utilize its behavior on both RF and LF and we propose a third HI capable of considering strains in the post-buckling regime. The new indicator is defined by combining the former health indicators (HI2) from both feet. As we can see from Figure 8, the health indicator presents a "mirrored" response regarding to the other foot. This is attributed to the anti-symmetric (with respect to the stiffener middle axis) first buckling eigen-mode of the panel (see insert graph at Figure 3a). Thus, the health indicator is defined as follows and diminishes the load dependency in the specific load range.

$$HI3_i = \frac{1}{2}[(HI2_i)^{RF} + (HI2_i)^{LF}] \tag{4}$$

where i stands for the FBG number, i = 1,..,5. This indicator now detects abnormal behaviors not at the exact spot that a sensor is mounted on a foot, but in the plane that two sensors are placed in corresponding locations of RF and LF. Again, a preliminary evaluation of this indicator is made by presenting the health indicators for the pristine model in the whole range of loads (Figure 10). The load values in the abscissa are normalized with the critical buckling load as derived by the nonlinear analysis. Proportionally to the load we observe that the health indicator HI3 shows negligible deviations. Next, the virtual strains have been acquired via the parametric analysis for a growing, centrally-placed disbond and the health indicators are illustrated in Figure 11. The indicators depicted are obtained from static strain data obtained in an array of load along up to 25 kN load that approximately equals 1.6 times the buckling load. We can clearly notice that the health indicator produces a monotonic behavior proportional to the disbond extent. The total increase is about 13.4%. Also, we can observe a gradient change in the rest indicators when the disbond size has increased so to approach the closely sensors of RFBG-3.

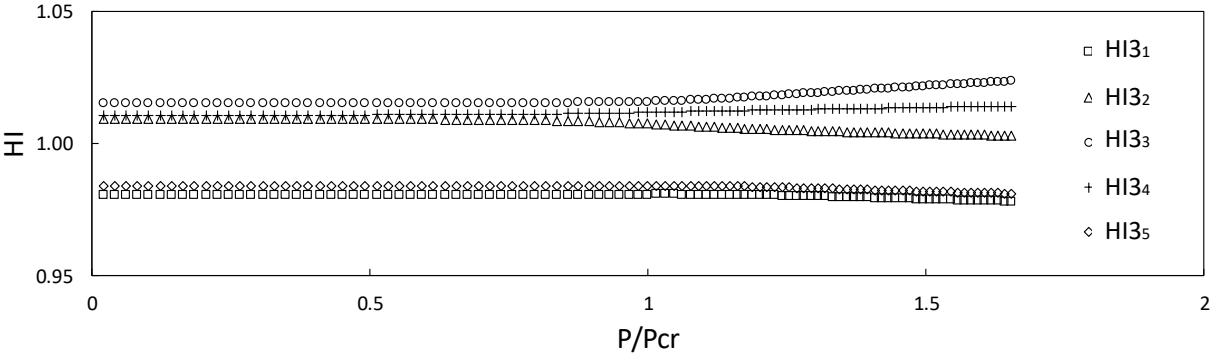

Figure 10. Virtually estimated HI3 indicators versus normalized load

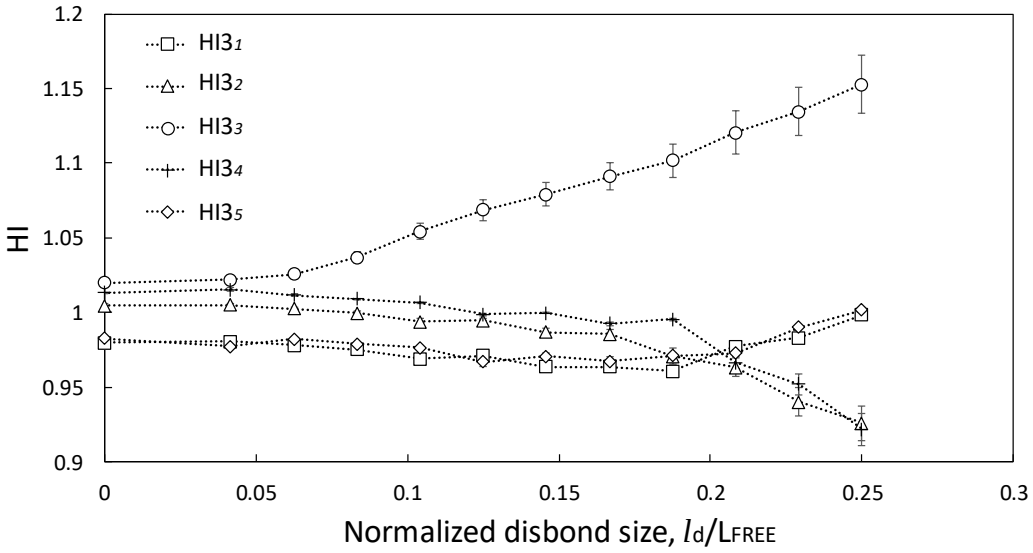

Figure 11. Average HI3 values of a half-width, centrally-placed disbond and various size configurations

4. Conclusions

In the current study, strain-based Health Indicators for skin/stringer disbonding monitoring of stiffened composite panels are investigated and evaluated. To achieve this aim and realize a plethora of damage scenarios, a parametric finite element analysis was conducted in order to simulate a single-stiffener composite panel subjected to uniaxial compressive loading. Longitudinal strains were computed at regions where in real-life permanent FBG sensors are foreseen to be attached. Initially, a non-linear finite element analysis was executed deriving the strains at various loads on the pristine (healthy) structure. Furthermore, several skin-to-stiffener disbonds of variable size and position were introduced via a parametric numerical modeling approach using Python® scripting.

First, a baseline-dependent method was investigated. For this purpose, a Health Indicator (namely HI1) was used comparing longitudinal strains of the pristine baseline with the disbonded cases. This indicator presented an increased sensitivity when the relevant strain acquisition point (e.g. FBG) was upon or closely placed to the subsurface disbonds. The primary drawback of HI1 is its load-dependency, making it difficult to be implemented when unknown or spectrum-like external loads act on a structural component.

A second health indicator HI2, which essentially represents a strain normalization scheme of every sensor measurement, was investigated and evaluated. By definition, this indicator is baseline independent as it does not take into consideration strains from the pristine structure. The evolution of this indicator was illustrated in a growing, artificially increased, disbond scenario and exhibited a monotonic behavior of the FBG sensor that was more affected by the disbond. In contrast to the first indicator HI1, the current HI2 presented a rather independent of the load value but only until buckling occurred. More specifically, when the structure transits to the buckling regime, the imminent bending of the skin and stringer feet produces

a non-constant strain distribution along the sensor bond-line per foot, as it is shown in Figure 6, following the single half-wave buckling mode of the SSP. Thus, the sensors develop different levels of strain and subsequently deviate from their initial (prior buckling) plateau proportionally to the load, with an anti-symmetrical relation between RF and LF, as it can be clearly noticed in Figure 8.

Hence, we propose a new health indicator, i.e. HI3, capable of the monitoring of T-joint single-stiffener panels imposed to compression. The proposed indicator synergistically combines the former HI2 from both feet in order to overcome its intrinsic dependency to load. This is achieved by leveraging on the behavior that HI2 presented at the two feet and dominantly attributed to the anti-symmetrically formed buckling shape of the panel. Moreover, the proposed HI3 could be potentially utilized for T-joint multi-stiffened panels, due to the fact that these structures buckle in an equivalent way to the single-stiffener panel, forming anti-symmetric buckling mode shapes. In cases where this symmetric mode shape of buckling behavior is not presented, for instance at hat-stiffened panels where symmetrical mode shapes are mainly formed, this indicator should be revisited to incorporate such a mode swift. Finally, HI3 demonstrated a load-independent behavior to an extended load range up to 1.6 times of the buckling load. The same indicator was assessed for the health monitoring of a growing disbond utilizing the parametric finite element model and revealed a promising monotonic behavior of the mainly affected FBG as the disbond size was virtually increasing. Moreover, it is baseline independent. In the future, we aim to assess the potential of the proposed Health Indicators during fatigue testing of single and multi-stiffener composite panels with artificially induced disbonds and/or impact damage.

Declaration of conflicting interests

The authors declared no potential conflicts of interest with respect to the research, authorship, and/or publication of this article.

Funding

The work presented in this paper was financially supported by the European Union's Horizon 2020 research and innovation programme ReMAP (Grant Agreement Number:769288). The support is appreciated by the authors.

References

Airoldi A, Bettini P, Loutas T, Koimtzoglou C and Sala G (2015) Design of health and usage monitoring systems based on optical fibers for composite wing spars. In: *28th ICAF Symposium*, Helsinki, Finland, 1-5 June 2015

Bisagni C and Vescovini R (2009) Analytical formulation for local buckling and post-buckling analysis of stiffened laminated panels. *Thin-Walled Structures* 47(3): 318-334.

Bisagni C, Vescovini R and Dávila CG (2010) Assessment of the Damage Tolerance of Post-Buckled Hat-Stiffened Panels using Single Stringer Specimens. In: *51st AIAA/ASME/ASCE/AHS/ASC Structures, Structural Dynamics, and Materials Conference*, Orlando, Florida, USA, 12-15 April 2010

Ciminello M, Concilio A, Galasso B and Pisano FM (2018) Skin-stringer debonding detection using distributed dispersion index features. *Structural Health Monitoring* 17(5):1245-1254.

Ciminello M, De Fenza A, Dimino I and Pecora R (2017) Skin-Spar Failure Detection of a Composite Winglet Using FBG Sensors. *Archive of Mechanical Engineering* 64(3).

Dávila CG and Bisagni C (2017) Fatigue life and damage tolerance of postbuckled composite stiffened structures with initial delamination. *Composite Structures*, 161(1): 73-84.

Fernández-López A, Menendez JM and Güemes A (2007). Damage Detection in a Stiffened Curved Plate by Measuring Differential Strains. In: *16th International Conference on Composite Materials*, Kyoto, Japan, 8-13 July 2007

Glisic B and Inaudi D (2012) Development of method for in-service crack detection based on distributed fiber optic sensors. *Structural Health Monitoring* 11(2): 161-171.

Grenestedt JL (1989) A study on the effect of bending-twisting coupling on buckling strength. *Composite Structures* 12(4): 271-290.

Güemes A, Fernández-López A and Soller B (2010) Optical Fiber Distributed Sensing - Physical Principles and Applications. *Structural Health Monitoring* 9(3): 233-245.

Hexcel Corporation (2016) HexPly® 8552 Product Datasheet. Available at: https://www.hexcel.com/user_area/content_media/raw/HexPly_8552_eu_DataSheet.pdf.(accessed 30 October 2019)

Hill KO and Meltz G (1997) Fiber Bragg Grating Technology Fundamentals and Overview. *Journal of Lightwave Technology* 15(8).

Katsikeros CE and Labeas G (2009) Development and validation of a strain-based Structural Health Monitoring system. *Mechanical Systems and Signal Processing* 23(2): 372-383.

Kenane M and Benzeggagh ML (1997) Mixed-mode delamination fracture toughness of unidirectional glass/epoxy composites under fatigue loading. *Composites Science and Technology* 57(5): 597-605.

Kesavan A, Sabu J and Herszberg I (2008) Strain-based Structural Health Monitoring of Complex Composite Structures. *Structural Health Monitoring* 7(3): 203-213.

Kolanu NR, Raju G and Ramji M (2018) Experimental and numerical studies on the buckling and post-buckling behavior of single blade-stiffened CFRP panels. *Composite Structures* 196: 135-154.

Krueger R (2004) Virtual crack closure technique: History, approach, and applications. *Applied Mechanics Reviews* 57(2): 109-143.

Li HCH, Beck F, Dupouy O, Herszberg I, Stoddart PR, Davis CE and Mouritz AP (2006) Strain-based health assessment of bonded composite repairs. *Composite Structures* 76(3): 234-242.

Li HCH, Herszberg I and Mouritz AP (2006). Automated Characterization of Structural Disbonds by Statistical Examination of Bond-line Strain Distribution. *Structural Health Monitoring* 5(1): 83-94.

Li HCH, Herszberg I, Mouritz AP, Davis CE and Galea SC (2004). Sensitivity of embedded fibre optic Bragg grating sensors to disbonds in bonded composite ship joints. *Composite Structures* 66(1-4): 239-248.

Loutas TH, Charlaftis P, Bettini P, Koimtzoglou C and Kostopoulos V (2015) Reliability of strain monitoring of composite structures via the use of optical fiber ribbon tapes for structural health monitoring purposes. *Composite Structures* 134: 762-771.

Milanoski DP and Loutas TH (2019) Strain-based damage assessment of stiffened composite panels for structural health monitoring purposes. In: *9th Thematic Conference on Smart Structures and Materials*, Paris, France, 8-11 July 2019

Palaniappan J, Ogin SL, Thorne AM, Reed GT, Crocombe AD, Capell TF and Mohanty L (2008) Disbond growth detection in composite-composite single-lap joints using chirped FBG sensors. *Composites Science and Technology* 68(12): 2410-2417.

Panopoulou A, Roulias D, Loutas TH and Kostopoulos V (2012) Health Monitoring of Aerospace Structures Using Fibre Bragg Gratings Combined with Advanced Signal Processing and Pattern Recognition Techniques. *Strain* 48(3): 267-277.

Romano F, Ciminello M, Sorrentino A and Mercurio U (2019) Application of structural health monitoring techniques to composite wing panels. *Journal of Composite Materials* 53(25): 3515-3533.

Salvetti M, Sbarufatti C, Cross E, Corbetta M, Worden K and Giglio M (2019) On the performance of a cointegration-based approach for novelty detection in realistic fatigue crack growth scenarios. *Mechanical Systems and Signal Processing* 123:84-101.

Sbarufatti C, Manes A and Giglio M (2013) Performance optimization of a diagnostic system based upon a simulated strain field for fatigue damage characterization. *Mechanical Systems and Signal Processing* 40(2): 667-690.

Shan Y, Xu H, Zhou Z, Yuan Z, Xu X and Wu Z (2019) State sensing of composite structures with complex curved surface based on distributed optical fiber sensor. *Journal of Intelligent Material Systems and Structures* 30(13): 1951-1968.

Sierra-Pérez J, Güemes A, Mujica L and Ruiz M (2015) Damage detection in composite materials structures under variable loads conditions by using fiber Bragg gratings and principal component analysis, involving new unfolding and scaling methods. *Journal of Intelligent Material Systems and Structures* 26(11): 1346-1359.

Takeda S-i, Aoki Y and Nagao Y (2012) Damage monitoring of CFRP stiffened panels under compressive load using FBG sensors. *Composite Structures* 94(3): 813-819.

Tian S, Yang Z, Chen X and Xie Y (2015) Damage Detection Based on Static Strain Responses Using FBG in a Wind Turbine Blade. *Sensors* 15(8): 19992-20005.

Worden K, Farrar RC, Manson G and Park G (2007) The fundamental axioms of structural health monitoring. *Proceedings of The Royal Society A*: *Mathematical, Physical and Engineering Sciences* 463(2082): 1639-1664.

Yashiro S, Wada J and Sakaida Y (2017) A monitoring technique for disbond area in carbon fiber-reinforced polymer bonded joints using embedded fiber Bragg grating sensors: Development and experimental validation. *Structural Health Monitoring* 16(2): 185-201.

Zarouchas DS and Alderliesten RC (2015) The effect of disbonds on stability aspects of adhesively bonded aluminum panels during compression loading. *Thin-Walled Structures* 96: 372-382.

Zou D and Bisagni C (2018) Skin-Stiffener Separation in T-Stiffened Composite Specimens in Postbuckling Condition. *Journal of Aerospace Engineering* 31(4).

The work presented in this paper was financially supported by the European Union's Horizon 2020 Research and Innovation Programme ReMAP under the Grant Agreement No:769288).